Physica B 666 (2023) 415114

Contents lists available at ScienceDirect

Physica B: Condensed Matter

journal homepage: www.elsevier.com/locate/physb

Synthesis and investigation of toxicity and photothermal effect of $NiFe_2O_4$@Cu core-shell nanoparticles

Nasim Yousefpour Novini [a], Kazem Jamshidi-Galeh [b], S.H. Reza Shojaei [a,c,*], Tavakkol Tohidi [d], Şahin Uyaver [e]

[a] Department of Physics, Faculty of Science, Sahand University of Technology, Tabriz, 51335-1996, Iran
[b] Department of Physics, Azarbaijan Shahid Madani University, Tabriz, Iran
[c] X-LAB, Hasselt University, Agoralaan, Diepenbeek, 3590, Belgium
[d] Northwest Research Complex (Bonab), Radiation Applications Research School, Nuclear Science and Technology Research Institute, Tehran, Iran
[e] Department of computer Engineering, Faculty of Technology, Marmara University, 34854, Maltepe, Istanbul, Turkey

ARTICLE INFO

Keywords:
Photothermal
Core-shell
$NiFe_2O_4$@Cu
Superparamagnetic
Toxicity

ABSTRACT

In this study, $NiFe_2O_4$ and $NiFe_2O_4$@Cu nanoparticles (NPs) were synthesized based on the co-precipitation method. The formation of cubic $NiFe_2O_4$ and $NiFe_2O_4$@Cu NPs was confirmed by the Bragg reflections in XRD analysis. The SEM images showed the distribution of the irregularly shaped agglomeration of $NiFe_2O_4$ and $NiFe_2O_4$@Cu NPs. The size distributions of the $NiFe_2O_4$@Cu samples with two different core shell thicknesses were mostly about 10.39 and 13.31 nm. The superparamagnetic nature of the synthesized NPs was verified by VSM at room temperature, and the NPs' saturation magnetization was found to be 37.04 emu/g, which was reduced after shielding the core. Furthermore, to investigate the cancer cell viability and cytotoxicity of the NPs on MCF7 breast cancer cells, different concentrations of NPs were examined. The response of the $NiFe_2O_4$@Cu NPs to the laser light irradiations indicated that these NPs can potentially be used for biomedical applications such as photothermal treatment.

1. Introduction

Depending on the structure and function of NPs, they can be synthesized in different forms, including simple, core-shell, and composite structures. By definition, core-shell NPs are made of inner material (core) and outer material (shell) [1,2]. In core-shell NPs, the core is mostly protected by the shell from unwanted reactions, e.g., oxidation, so the core is more stable when there is a shell. Depending on application, the core and shell of core-shell NPs can be selected from a variety of existing elements or composites comprising organic-organic, organic-inorganic, inorganic-organic, and inorganic-inorganic materials. Among the listed interactions, the first one (inorganic-inorganic) is frequently used [1]. Besides, different parameters, such as size, shape, and synthesis procedure, can highly affect the individual properties of these types of materials. Core-shell NPs have been extensively studied in different disciplines including biology and biomedicine [3]. The magnetic NPs that have been studied so far owe their irregular properties to nano dimensions, which are smaller than the corresponding critical diameter. The critical diameter varies in different magnetic materials [4]. For example, the critical diameters of $NiFe_2O_4$ have been reported to be 10–25 nm [5]. One of the most important features of finite size is superparamagnetism [6], which is characterized by zero magnetic residual, zero coercivity, high susceptibility, and high saturation [7]. In such a system, the magnetic moment is parallel to the easy axes of the superparamagnetic materials, and the anisotropic energy is zero. Moreover, due to the lack of the domain wall and energy exchange, the total energy is minimal, and only the magnetostatic energy is valid [8]. These fantastic exceptional properties of these materials make them promising for biomedical uses, especially in photothermal (also known as hyperthermia), drug delivery, and Magnetic Resonance Imaging (MRI) [9,10]. Considering the possibility of killing or blocking the superficial and deep-seated [11] cancerous cells based on a hyperthermia treatment that uses magnetic NPs, this technique has widely attracted the attention of researchers [12,13].

$NiFe_2O_4$ superparamagnetic NPs (SPNPs) absorb light in a wider range: from the visible to the NIR part of the electromagnetic spectrum. The energy absorption of $NiFe_2O_4$ NPs in the NIR region can be exploited to convert electromagnetic energy to heat. on the other hand, small

* Corresponding author. Department of Physics, Faculty of Science, Sahand University of Technology, Tabriz, 51335-1996, Iran.
E-mail address: shojaei@sut.ac.ir (S.H.R. Shojaei).

https://doi.org/10.1016/j.physb.2023.415114
Received 27 April 2023; Received in revised form 18 June 2023; Accepted 3 July 2023
Available online 5 July 2023

SPNPs exhibit greater cellular internalization and deeper penetration into multicellular spheroids, enabling a higher efficacy of photothermal ablation under in-vitro conditions. Interestingly, larger SPNPs show greater accumulation in tumors, which increases their ability in efficient tumor growth inhibition [14].

Photothermal is a more precise and less invasive treatment than magnetic hyperthermia. The reason for this precision lies in some characteristics of the laser source used in this method. The power tunability to control the temperature of the cell [15], easy operation, and the capability of being locally focused on a specific region of the target are some of the advantages of photothermal. Moreover, those patients who have limitations to use MRI scan, will not be able to use magnetic hyperthermia for cancer treatment. For example, those patients with implanted devices sensitive to magnetic fields (e.g., pacemakers) cannot be treated by the external magnetic field. High-intensity magnetic fields might bring other potential risks to these patients [13]. Despite far fewer side effects of photothermal compared to other treatments (e.g., chemo, radiotherapy, and magnetic hyperthermia), a combination of photothermal and chemo or radiotherapy is employed to have better treatment results [9,16].

The heat generated by the photothermal NPs under laser irradiation is fully transferred to the cancer cells, so the potential damage to the surrounding healthy cells and tissues is remarkably reduced [12,17]. The best temperature ranges to kill cancerous cells and to keep healthy tissues is between 40 and 46° Celsius [9], while in temperatures above 47, it is highly possible that healthy cells lose their functionality through protein degradation and DNA damage [18].

Due to their chemical stability, low cost and affordability of reagents, and simple synthesis procedure [19,20], materials with the general formula, MFe_2O_4 (M = Zn, Ni, …), known as ferrites, are the best candidates for photothermal hyperthermia [21]. Among ferrites, $NiFe_2O_4$, which has been categorized as a soft ferrite [22], is highly preferred because the temperature of the target can effectively be controlled. Moreover, $NiFe_2O_4$ has high Curie temperature, environmental stability, and high electrical resistivity [23,24]. Ideal photothermal agents not only absorb energy in the near-infrared (NIR) range but also have a high photothermal conversion efficiency [13].

The heating capability of magnetic NPs including magnetite (Fe_3O_4) and maghemite (γ-Fe_2O_3) NPs has been investigated by several research groups. Due to their biocompatibility, these materials seem to be very promising candidates for biomedical applications. However, a very limited number of studies have focused on other types of ferrites [12].

The copper (Cu) existing in biomaterials appears in two major forms, i.e., ionic and metallic. Both types exhibit unique conductance and antibacterial characteristics [25]. Up to now, copper has been extensively studied in treatments and copper-based anticancer approaches. Moreover, due to the high heating photothermal efficiency of copper oxide NPs, this material is a potential candidate for theragnostic approaches [26,27].

In 2020, Diana Saikova reported a successful core-shell particle synthesis using a thick gold shell and a magnetic $NiFe_2O_4$ core for applications in cell isolation, MRI, targeted drug delivery, and hyperthermia. The results showed that $NiFe_2O_4$@Au has a magnetic response similar to standard superparamagnetic NPs and is consistent with the magnetic behavior of $NiFe_2O_4$ NPs without the gold shell. It was also pointed out that this approach can be generalized to other iron oxides and metal ferrites [28]. In 2020, Changyuk Ko investigated the photothermal and magnetic hyperthermia properties of Fe@Fe_3O_4 NPs under an infrared laser at 808 nm and a magnetic field at 150 kHz in a wide range of magnetic field strengths (140–180 Oe). The Fe@Fe_3O_4 NPs showed a photothermal effect above 20 °C after 5 min at 1 W of NIR irradiation and a constant temperature rise rate during 5 cycles. Additionally, their results showed that the Fe@Fe_3O_4 NPs can be used in biomedical applications [29].

In 2021, Xuan Gao showed that $Cu_{1.2}O$ NPs have a significant potential for photothermal due to their high NIR absorption and good biocompatibility. Moreover, these NPs with satisfactory T_1 relaxation coefficient (r_1) can be effectively used as unique MRI contrast agents and have shown excellent response for MRI applications [27].

In this work, $NiFe_2O_4$ and $NiFe_2O_4$@Cu NPs are prepared by the simple and low-cost method of co-precipitation. The optical, morphological, and structural properties of the NPs are investigated. The influence of the shell layer thickness and different concentrations of the $NiFe_2O_4$@Cu NPs on the photothermal characteristics are studied. Besides, the cytotoxicity of the $NiFe_2O_4$@Cu NPs is reported. Although $NiFe_2O_4$ NPs were investigated in magnetic targeting and imaging process but, to the best of the authors' knowledge, the photothermal effect of $NiFe_2O_4$ NPs was not studied so far. However, $NiFe_2O_4$ NPs, on their own are photothermal agents but to improve their photothermal functionality, they have been coated by copper which is considered as a good absorbent in UV-NIR region.

2. Experimental details

The grade of all chemicals was analytical (Sigma-Aldrich). These chemicals were not further purified and used as received.

2.1. Synthesis of $NiFe_2O_4$NPs

This study used the co-precipitation method for the synthesis of the $NiFe_2O_4$ NPs. Nickel nitrate and iron nitrate were used as the source materials. First, 10 mL of $Ni(NO_3)_2$ (0.4 mol/L) was added to 10 mL of $Fe(NO_3)_3$ (0.8 mol/L) to prepare a mixture. Then, 0.5 mL of TA (0.1 mol/L, tartaric acid) and 0.0728 g of CTAB (cetrimonium bromide) were added to the solution as stabilizer and surfactant, respectively. After that, 1 mol/L of NaOH was added dropwise to the solution until the solution PH reached 10. Meanwhile, the mixture was stirred via a magnetic stirrer, which was set to 1000 rpm for 2 h at 40 °C. A product in brown color was collected by using an external magnet for excess surfactant (spurious phases) removal, and the precipitate was centrifuged three times for about 15 min (Fig. 1). Finally, the product was washed with distilled water (to reach neutral pH) and dried for 2 h in the air at 80 °C. To improve the crystalline conditions of the samples, they were put in a muffle furnace at 580 °C for 3.5 h. The $NiFe_2O_4$ NPs were precursor materials.

2.2. Copper shell formation

The preparation process of the $NiFe_2O_4$@Cu NPs is illustrated in Fig. 2. The Cu shell deposition onto the $NiFe_2O_4$ surface was controlled or directed via the chemical reduction of the mercaptoacetic acid (MAA) in the suspension of the $NiFe_2O_4$ NPs. Then, 50 μL MAA was added to 25 mg $NiFe_2O_4$ NPs in water solution (20 mL) under shaking for 12 h. Next, the MAA-functionalized $NiFe_2O_4$ NPs were collected with a magnet followed by twice washing with distilled water and ethanol. The MAA-functionalized $NiFe_2O_4$ NPs were interspersed in 30 mg $Cu(CH_3COO)_2$ and 0.2 M $NaBH_4$ of ethanol solution (20 mL). The process of deposition was carried out for 45 min at 30 °C with continuous stirring at 800 rpm. The magnetic nanoparticles (MNPs) were centrifuged and washed with distilled water two times (Fig. 2). In the end, these MNPs were interspersed in ethanol for further investigations. The copper deposition procedure was repeated twice under the same settings. From now on, $NiFe_2O_4$@Cu(1) and $NiFe_2O_4$@Cu(2) are referred to as single and double coating NPs, respectively.

2.3. Characterization

The crystal structure of the materials was analyzed by a Panalytical diffractometer (1.5406 A, Cu K-alpha, made by X'Pert Pro, Netherlands). An FE-SEM (Tescan, MIRA3 FEG) was used to examine the NPs morphology. Photothermal evaluation of solutions was performed in the NIR range using an 808 nm laser (FAP diode laser). TEM images were

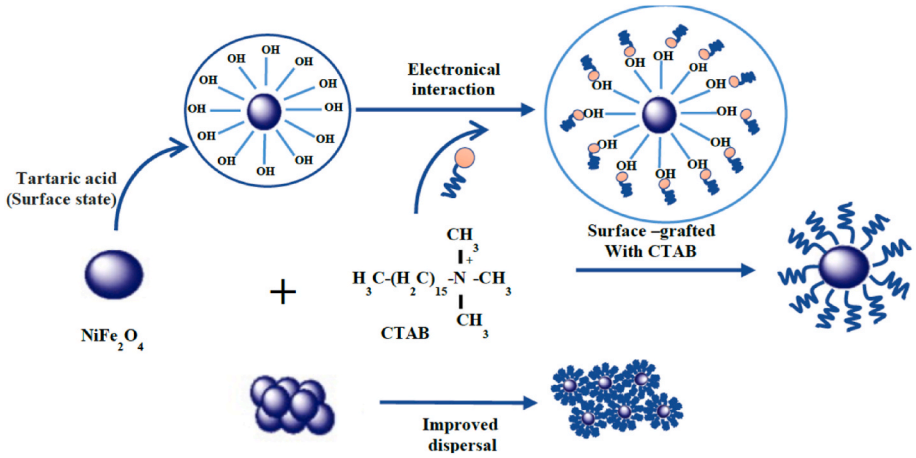

Fig. 1. Functionalization of the $NiFe_2O_4$ NPs.

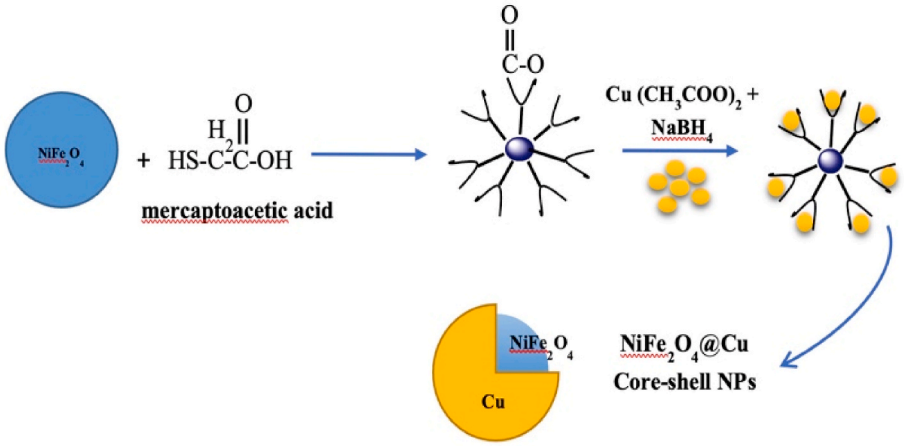

Fig. 2. Synthesis route of $NiFe_2O_4$@Cu NPs.

obtained using an HR-TEM (TEC9G20 USA-FEI) at 200 kV accelerating voltage. Magnetic measurements were performed at room temperature using a VSM (MDK, Magnetism Daneshpozheh Kashan Company) with a maximum magnetic field of 15 kOe. The photoluminescence (PL) characteristics were measured by an FP-6200-type spectrofluorometer (JASCO Corporation, Tokyo, Japan). To study the photoluminescence of the MNPs, 15 mg of the samples was dispersed in 10 mL of ethanol.

3. Results and discussion

3.1. XRD results

The XRD spectra of $NiFe_2O_4$, $NiFe_2O_4$@Cu(1) and $NiFe_2O_4$@Cu(2) are shown in Fig. 3. The XRD patterns of the samples show well-defined and broad peaks, indicating the fine grain size and crystalline nature of the synthesized materials (Fig. 3). The 2θ values of peaks at 30.5°, 35.88°, 37.02, 43.51°, 54.07°, 57.64°, 63.16°, and 72.01°, correspond, respectively, to the (220), (311), (222), (400), (422), (511), (440) and (620) planes of the cubic phase of $NiFe_2O_4$ (JCPDS files no. 03–0875). The characterized peaks appear at 43.51°,50.5°, and 75.01°, which can be attributed, respectively, to the (111), (200), and (220) planes of Cu (JCPDS files no. 969012044). The preferred growth orientation for all samples is (311), but the intensity of the (311) peak decreases with the increase in the shell layer thickness. Furthermore, the crystallite size of the NPs increases after single and double coating [28–30].

There are many methods for calculating the crystallite size of NPs,

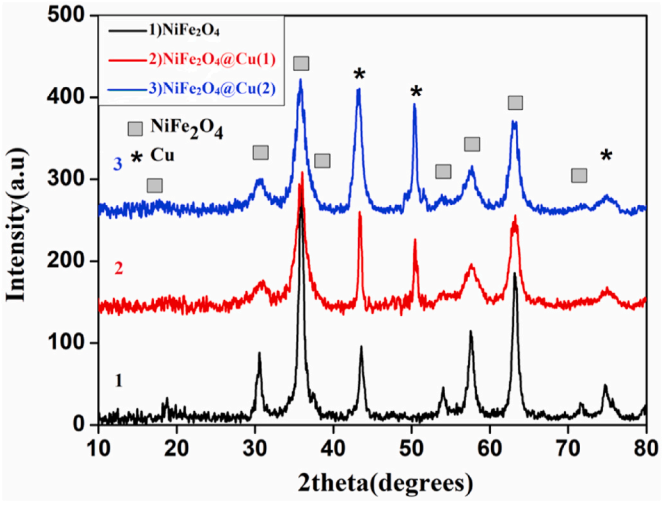

Fig. 3. XRD patterns of $NiFe_2O_4$, $NiFe_2O_4$@Cu(1), and $NiFe_2O_4$@Cu(2)

such as the Debye-Scherrer and Williamson-Hall methods. In the Scherrer method, the crystallite size is estimated using the maximum intensity of the diffraction peak in the XRD pattern, and this method assumes that the broadening of the diffraction peak is due to the crystallite size. However, the Williamson-Hall method presumes that the

width and intensity of Bragg peaks are related to both crystallite size and lattice defects. The lattice defects, which can be caused by lattice displacement, the presence of impurities and lattice dislocation, put stress and strain on the crystal lattice.

Now, the crystallite size can be obtained by Debye–Scherrer equation (Eq. 1):

$$D = \frac{0.9\lambda}{\beta \cos\theta} \quad (1)$$

Furthermore, the strain values and crystallite size of the samples are calculated using the Williamson-Hall equation (Eq. 2):

$$\beta\, Cos(\theta) = \varepsilon \times 4\, \sin(\theta) + \frac{k\lambda}{D} \quad (2)$$

where β, ε, λ, θ, and D are the full width at half maximum of the peak (in radians), the value of strain, the wavelength (1.5406 Å), the diffraction angle, and the crystallite size, respectively.

A plot is drawn in Fig. 4 with $4sin\theta$ along the x-axis and $\beta cos\theta$ along the y-axis for the NPs. From the linear fit to the data, the crystallite size was estimated from the y-intercept, and the strain ε, from the slope of the fit. Table 1 shows the average crystallite sizes of $NiFe_2O_4$, $NiFe_2O_4$@Cu(1), and $NiFe_2O_4$@Cu(1), which were estimated to be respectively 9.4, 10.97, and 13.05 nm, in the Scherrer method. At the same time, the average crystallite sizes were 13.16, 14.33, and 15.23 nm based on the Williamson-Hall method. The results clearly show the difference between these two methods, which is due to considering the strain in the crystal structure [31].

Table 1
Crystallite size and strain of the NPs based on the co-precipitation method.

Sample	Williamson-Hall method		Average crystallite size by Scherer method (nm)
	Strain	Average crystallite size (nm)	
$NiFe_2O_4$	0.0036	13.16	9.4
$NiFe_2O_4$@Cu (1)	0.0003	14.33	10.97
$NiFe_2O_4$@Cu (2)	0.00004	15.23	13.05

3.2. FE-SEM and EDX patterns

For morphological characteristics of the NPs (Fig. 4a–c), an FE-SEM was used. Insets of Fig. 5a-c shows the particle size distributions of the samples obtained by the ImageJ software. As shown, the FE-SEM of the spherical grains of $NiFe_2O_4$, $NiFe_2O_4$@Cu(1), and $NiFe_2O_4$@Cu(2) have average crystallite sizes of 14.03, 15.20, and 16.31 nm, respectively. It is worth mentioning that the average crystallite sizes estimated by FE-SEM are significantly larger than those obtained in the XRD analysis. This is because many crystals are identified as secondary particles instead of single crystals [32].

The elemental compositions of the samples were analyzed by EDX. Fig. 5d indicates the presence of Ni, Fe, and O in all samples, which proves the formation of $NiFe_2O_4$. Further, the EDX results of $NiFe_2O_4$@Cu(1) and $NiFe_2O_4$@Cu(2) show the presence of Cu. All these

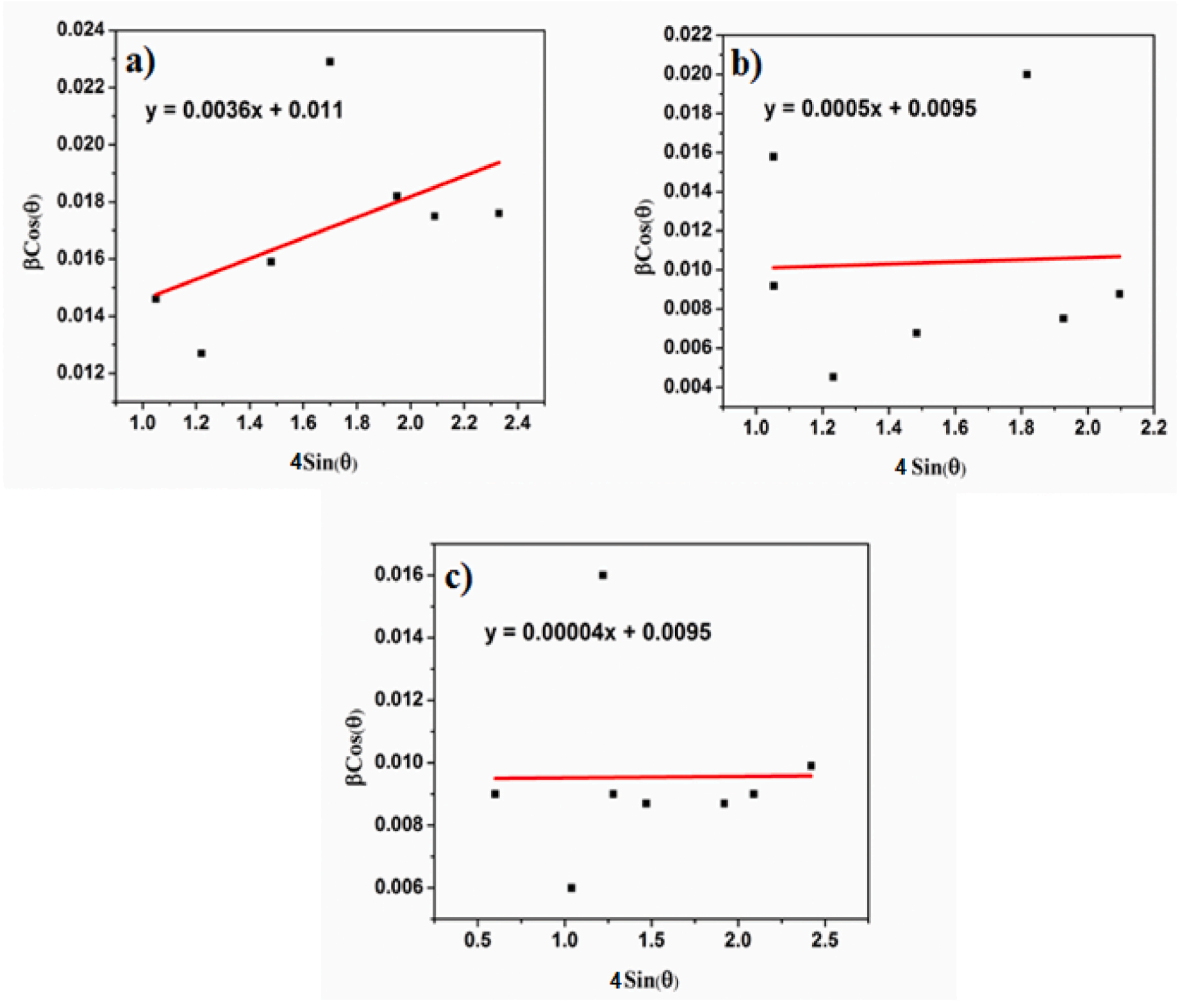

Fig. 4. Particle size distribution of a) $NiFe_2O_4$, b) $NiFe_2O_4$@Cu(1), and c) $NiFe_2O_4$@Cu(2) according to the Williamson-Hall method.

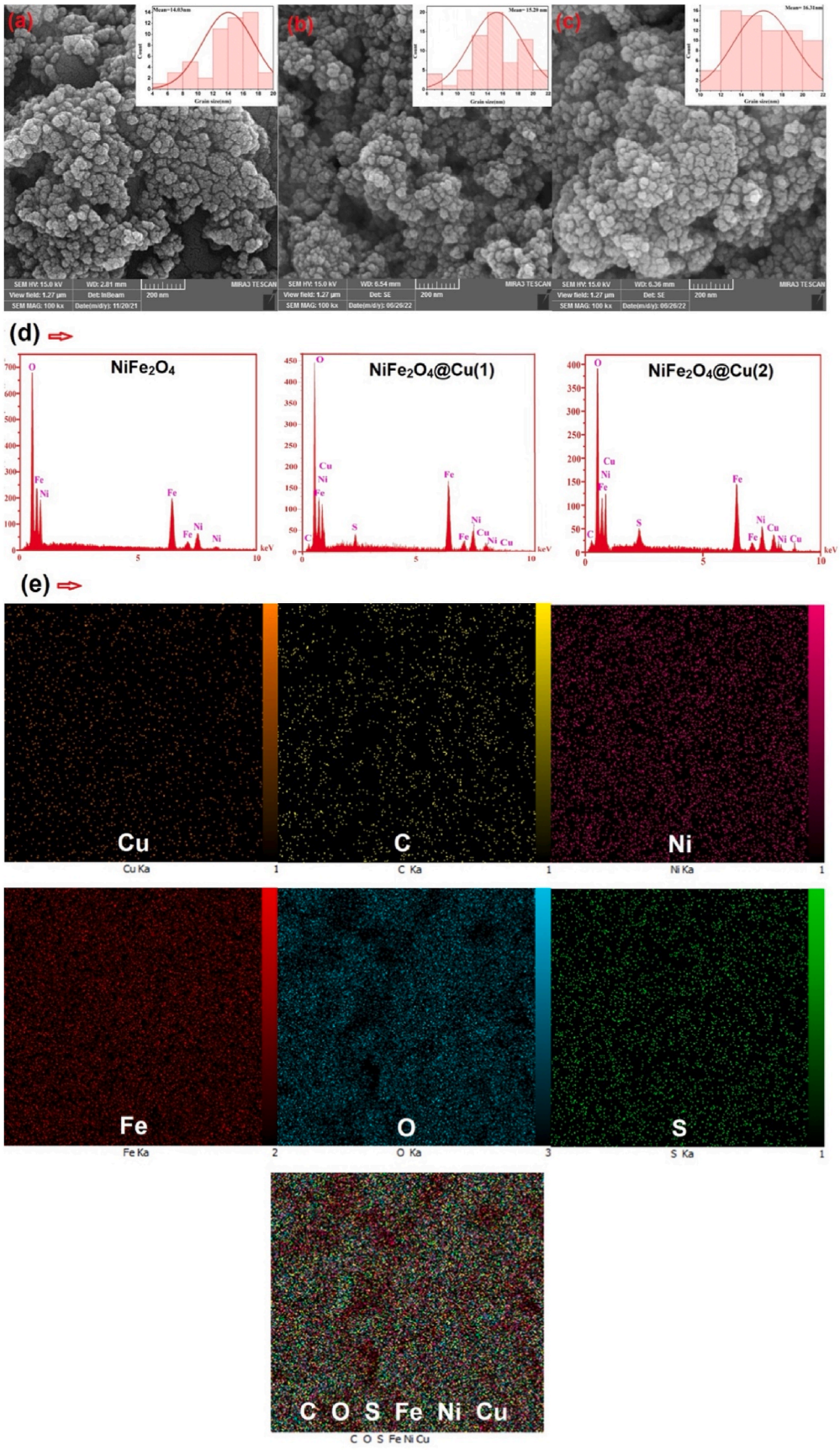

Fig. 5. (a–c) FE-SEM images of $NiFe_2O_4$, $NiFe_2O_4$@Cu(1), and $NiFe_2O_4$@Cu(2), respectively (Inset: particle size distributions); (d) EDX of samples and (e) Elemental mapping micrograph of $NiFe_2O_4$@Cu(1)

findings clearly show the successful production of core-shell material without any impurities [33,34]. The EDX elemental mapping of the $NiFe_2O_4$@Cu(1) is presented in Fig. 5e. The EDX analysis of $NiFe_2O_4$@Cu(1) confirms the presence of the Ni, Fe, O, Cu, C and S signals, which indicate the purity of the samples. A similar distribution of the elements can confirm the successful formation of the $NiFe_2O_4$@Cu. Moreover, analyses were done at different points on compositions, and no significant changes were found from point to point. This confirms that the implemented synthesis method is effective for the preparation of the core-shell NPs with homogeneous compositions. Also, there is no accumulation of elements because in chemical synthesis methods (bottom-up production methods), materials are mixed at the molecular level [35].

3.3. TEM studies

Morphological studies, i.e., particle size distribution, particle shape, SAED pattern, and HR-TEM image of the synthesized $NiFe_2O_4$@Cu(1) and $NiFe_2O_4$@Cu(2) NPs are shown in Fig. 6(a–d). According to the TEM patterns (insets of Fig. 6a and b), the final $NiFe_2O_4$@Cu magnetic NPs are composed of a Cu shell and a $NiFe_2O_4$ core, indicating core-shell NP formation. The HR-TEM images indicate a quasi-spherical structure for some of the particles and irregular shapes for others (Fig. 6a and b). It is evident that the irregular shapes of the particles are due to the agglomeration of the particles, which may be related to the magnetic nature of the two components (Fe and Ni) that form the core, preparation method, and NPs surface properties [35]. Furthermore, the shell thickness of the prepared $NiFe_2O_4$@Cu increases gradually with increasing Cu coating number. The average shell thickness is 2.16 nm for $NiFe_2O_4$@Cu(1) and 4.45 nm for $NiFe_2O_4$@Cu(2), suggesting that by varying the coating number, the thickness of the Cu shell can be adjusted (insets of Fig. 6a and b) [36]. These images indicate that the $NiFe_2O_4$@Cu NPs obtained by this method are uniform in both crystallite size and morphology. The ImageJ software was used for grain size analysis and the size distributions as presented in Fig. 6a and b. The average crystallite sizes of $NiFe_2O_4$@Cu(1) and $NiFe_2O_4$@Cu(2) were

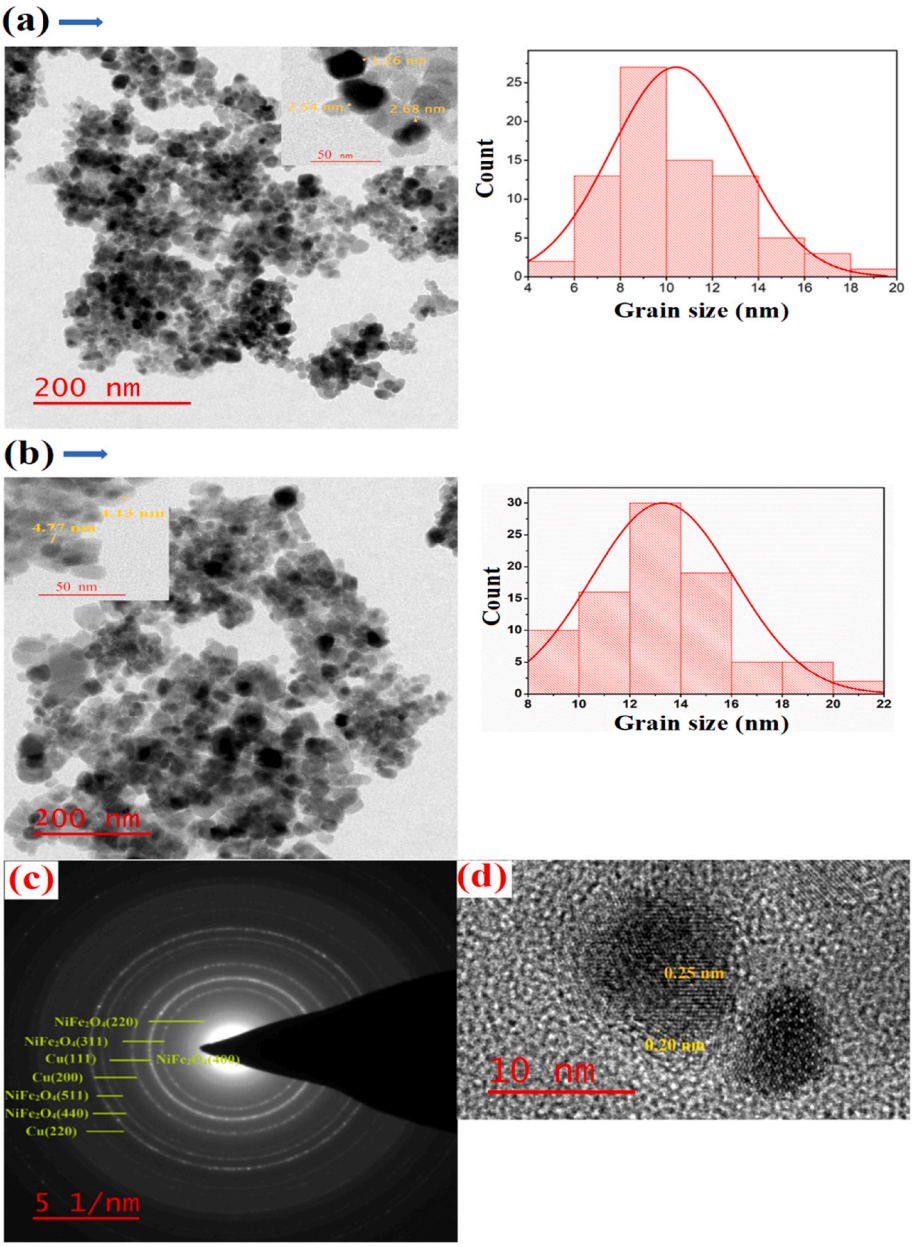

Fig. 6. (a) TEM images and particle size distributions of $NiFe_2O_4$@Cu(1) and (b) $NiFe_2O_4$@Cu(2); (c) SAED pattern and (d) HR-TEM images of $NiFe_2O_4$@Cu(1)

estimated to be 10.39 nm and 13.31 nm, respectively, which are in good agreement with those of the XRD analysis.

The SAED of the $NiFe_2O_4$@Cu(1) is shown in Fig. 6c. The appearance of the well-defined diffraction rings are related to the (220), (311), (400), (511), and (440) planes for $NiFe_2O_4$, and the (111), (200), and (220) planes for Cu. These results are in good agreement with the results of the structural investigations carried out by the XRD technique discussed earlier [31,37]. In addition, the SAED pattern shows the bright rings increased in diameter, indicating the crystalline nature of the sample.

An HR-TEM image of the $NiFe_2O_4$@Cu(1) is shown in Fig. 6d, which reveals lattice fringes of the (311) and (111) planes with the lattice spacings of 0.25 nm and 0.20 nm for $NiFe_2O_4$ and Cu, respectively [17,38,39]. The presence of lattice fringes indicates that the $NiFe_2O_4$@Cu nanoparticle is fully crystalline.

3.4. VSM studies

The magnetic properties, which are related to NPs size, can be evaluated by VSM. Fig. 7 shows the magnetic response of the $NiFe_2O_4$, $NiFe_2O_4$@Cu(1) and $NiFe_2O_4$@Cu(2) NPs in the presence of external fields in the range from −15 to 15 kOe. It is clearly seen that the hysteresis and coercive fields tend to zero and vanish, so the superparamagnetic properties are confirmed. This phenomenon is often observed when the size of magnetic particles decreases to the critical diameter [40]. According to the results in Table 2, the saturation magnetization of the $NiFe_2O_4$ NPs is equal to 37.04 emu/g; however, due to the broken exchange interactions in the surface layers and the local chemical disorder of NPs, this value is less than the value reported for the bulk [41]. Likewise, the values related to the saturation magnetizations of the single and double coatings are obtained to be about 23.86 and 17.68 emu/g, respectively. The saturation magnetization is reduced with coating due to two reasons. The first one is the weight contribution of the non-magnetic copper material, and the second one can be explained by the dead layer theory. In this theory, the magnetic materials are assumed to be protected by a non-magnetic layer, while the surface spins are disordered [26,42–44]. The magnetic moment (η_B) of the $NiFe_2O_4$ NPs is calculated using equation (3) [33,45]:

$$\eta_B = \frac{M_s \times M_w}{5585} \tag{3}$$

where 5585, *Ms,* and M_w are the magnetic factor, saturation magnetization, and molecular weight, respectively. Now, according to the value of saturation magnetization of the $NiFe_2O_4$ NPs, we obtain a magnetic moment of 1.52 for these NPs.

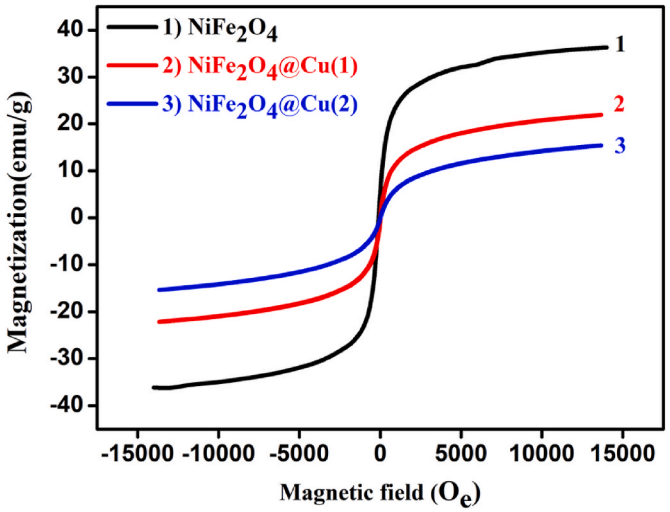

Fig. 7. VSM results of $NiFe_2O_4$, $NiFe_2O_4$@Cu(1) and $NiFe_2O_4$@Cu(2)

Table 2
Saturation magnetization (M_s) of $NiFe_2O_4$, $NiFe_2O_4$@Cu(1), and $NiFe_2O_4$@Cu(2)

Sample	$NiFe_2O_4$	$NiFe_2O_4$@Cu(1)	$NiFe_2O_4$@Cu(2)
M_s (emu/g)	37.04	23.86	17.68

3.5. Optical studies

Absorption spectra are useful parameters for investigating the optical properties of various materials. Fig. 8 shows the optical absorption of the prepared $NiFe_2O_4$, $NiFe_2O_4$@Cu(1), and $NiFe_2O_4$@Cu(2) NPs in the wavelength range of 200–1200 nm. In the absorption spectra of the

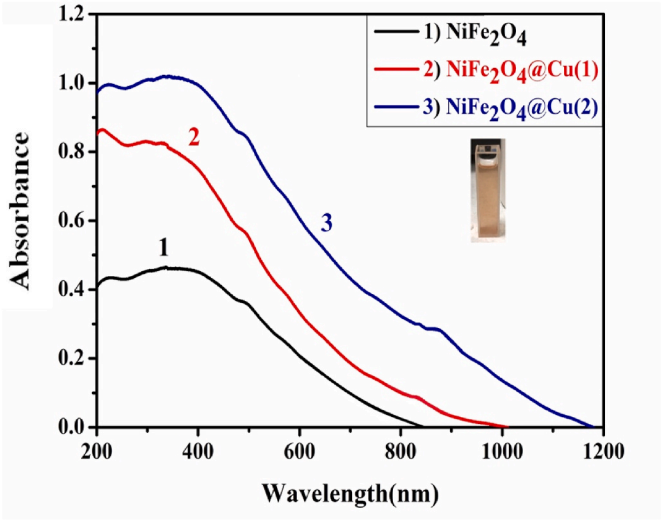

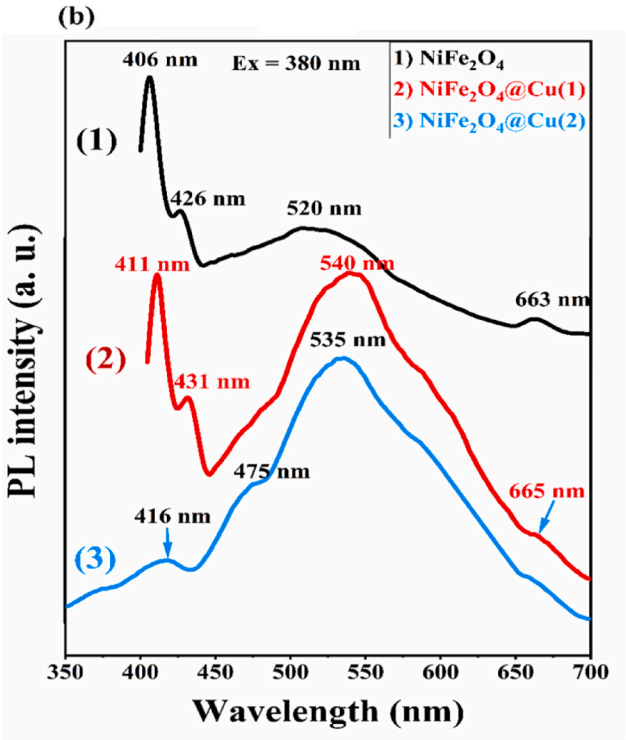

Fig. 8. (a) UV–Vis spectra and (b) PL spectra of $NiFe_2O_4$, $NiFe_2O_4$@Cu(1), and $NiFe_2O_4$@Cu(2)

samples, there is a continuous widespread absorption that is gradually reduced as the wavelength increases. Also, with increasing Cu shell thickness, the absorption increases. This may be due to the increasing NP particle size. Moreover, in the visible region (about 500 nm) the copper has absorption peak. As we know, the nickel ferrite also has absorption peak about 500 nm. So, the overlap take place, and these peaks cannot be identified individually. In addition, there is a peak in IR region (about 900 nm), which represents Cu absorption [46,47].

Fig. 8b shows the photoluminescence (PL) spectrum at room temperature and under excitation at 380 nm for the synthesized samples. The emission peaks are located in the visible region between 406 and 650 nm for the synthesized samples. The PL emission peaks are observed at 406, 426, 520, and 663 nm for the $NiFe_2O_4$ NPs. The PL peaks for $NiFe_2O_4$@Cu(1) are detected at 411, 431, and 540 nm, and a shoulder is observed at 665 nm. The $NiFe_2O_4$@Cu(2) sample has two sharp emission peaks at 416 and 535 nm as well as two shoulders at 475 and 665 nm. For $NiFe_2O_4$@Cu(1,2) samples, the PL intensity decreases, and the emission peaks shift to higher wavelengths. Furthermore, in the presence of the Cu shell, PL quenching occurs as a result of efficient transport of photogenerated electrons from $NiFe_2O_4$ to Cu shell [48].

The electronic configurations of Ni^{2+} ion with ^3F ground state and Fe^{3+} ion with ^6S ground state are $^3d_8$ and $^3d_5$, respectively. The emission peaks at around 406, 411, and 416 nm can be due to the near band edge transition of free electrons and the high density of oxygen vacancies [49]. The emission peaks that appear at 426, 431, and 475 nm of the PL spectrum can be attributed to the $^3A_2(^3F) \rightarrow {}^3T_1(^3P)$ and $^3A_2(^3F) \rightarrow {}^1T_2(^1D)$ transitions of Ni^{+2} in octahedral sites. The bands located at 520, 535, and 540 nm (widespread emission peaks centered in the green region) can be ascribed to the transition $^3d^5 \rightarrow 3\ d^4\ 4s$ of Fe^{+3} ions. In this case, an electron is excited to the conduction band formed predominantly by the 4s orbital of Fe^{+3} from the localized 3 d^5 state of Fe^{+3}. However, the bands located at 663 and 665 nm are attributed to Fe^{3+} in the tetrahedral sites [50].

3.6. Photothermal effect studies

To measure the thermal characteristics of the prepared NPs under NIR laser irradiation, different concentrations (1–5 mg) of NPs are dispersed in 1 mL of water and transferred to an optical cuvette. Then, samples at each NP concentration are irradiated by a NIR laser with power values of 1 W, 1.5 W, and 2 W at 808 nm. The temperature variation of the solution is determined using an optical thermometer with measurements recorded every 30 s. Fig. 9 shows a setup for measuring photothermal effect performance. Three important parameters such as concentration of the solution, laser power, and irradiation time are adjusted during the test and the relationships between these parameters are investigated.

From the results in Fig. 10a & b, the solution temperature can be exactly controlled from 23.5 to 47.5 °C related to $NiFe_2O_4$, $NiFe_2O_4$@Cu, and different concentrations of $NiFe_2O_4$@Cu(2) NPs. It can be observed that the photothermal effect is adjustable for these NPs. The temperature variation of the dispersion corresponding to 5 mg concentration of the NPs is recorded as a function of time at different laser powers to further investigate the photothermal performance of the NPs (Fig. 10c & d). It should be noted that these measurements were made until the system reached a stable state. At the beginning of temperature variations, since the temperature increases linearly proportional to the irradiation time, it can be concluded that the emitted laser beam is absorbed to some extent regardless of its intensity. It has even been reported that this phenomenon results from the heat exchange between the surroundings and the solution [26]. The recorded temperature variations increase with the increase in the copper shell thickness, so this can be attributed to the wide absorption of copper in the NIR region (808 nm) [27]. In addition, these temperature variations increase with the increase in $NiFe_2O_4$@Cu(2) concentration as a result of the presence of a large number of NPs in the aqueous suspension. The temperature of the sample increases due to the increased solution concentration, laser power, and irradiation time. In the meantime, we use the following simple formulas to calculate heat generation and heat conversion efficiency.

$$C = W_w C_w + \sum W_i C_i \tag{4}$$

$$\text{Heat generation} = C \cdot \Delta T \tag{5}$$

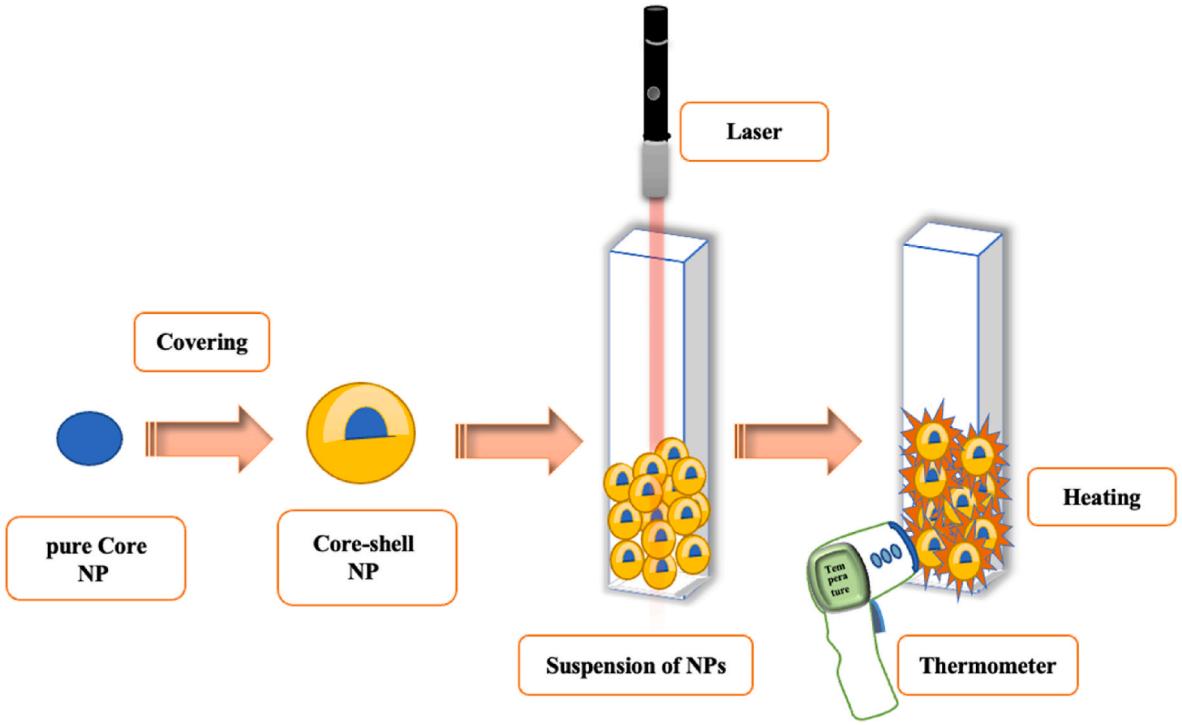

Fig. 9. Set-up for measuring photothermal effect performance.

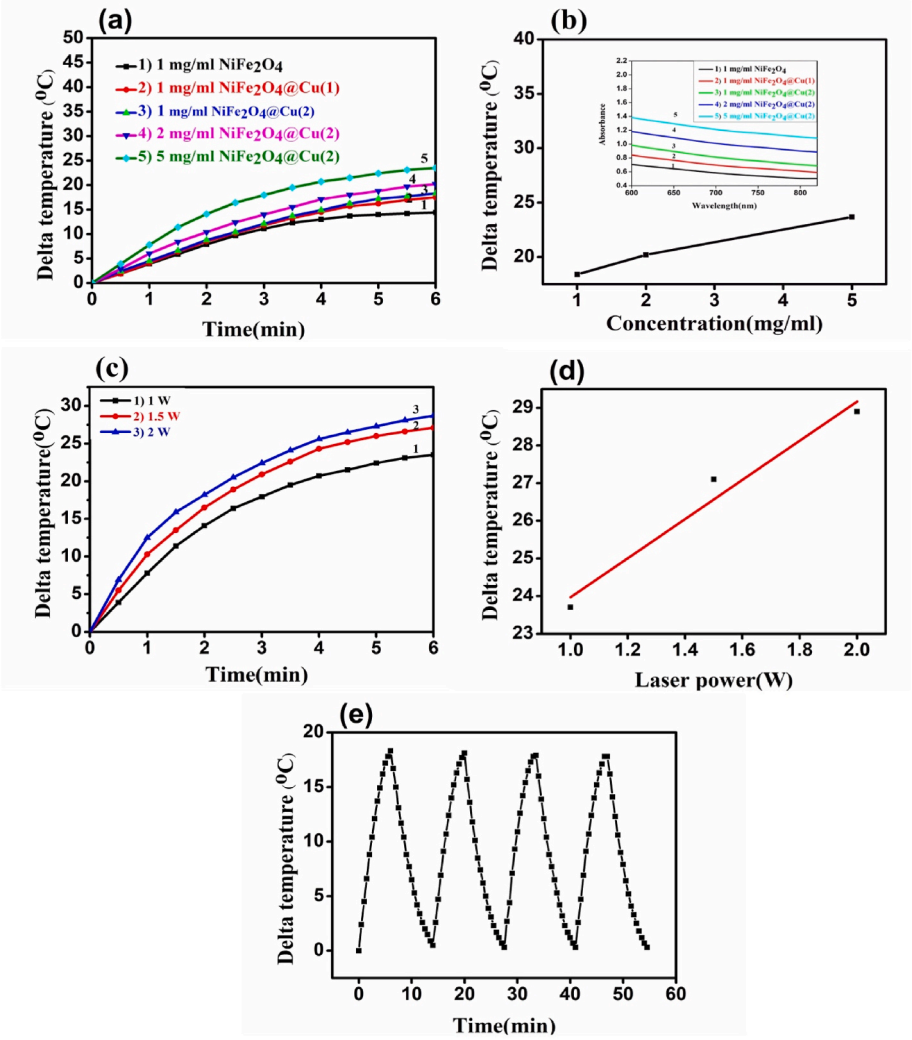

Fig. 10. Photothermal effect characteristics of the NPs, a/b) (1–5 mg/mL) concentrations, c/d) laser power, and e) cycle test for 2 mg/mL $NiFe_2O_4$@Cu(2)

$$\text{Efficiency} = \frac{C \cdot \Delta T}{\text{Irradiated energy}} \tag{6}$$

where W_w, W_i, C, and T are the mass fraction of water, mass fraction of solute, heat capacitance of the solution [50] (4.15–4.17 J/g.K), and temperature in degrees Celsius, respectively. During the initial phase of heating (where heat dissipation can be neglected), the irradiant energy can be written as $I_0 \cdot (1 - 10^{-A})\ \Delta t$, where I_0 (W) is the incident laser power, A is the absorbance of the sample at the irradiation wavelength that the 10^{-A} becomes negligible at high concentration [13,51].

Therefore, the photothermal conversion efficiency reaches 16.2%–27.6% according to the concentration of the solution [13,27,28,52]. We performed a cycle test for 2 mg/mL $NiFe_2O_4$@Cu(2) under 1 W and found that the same photothermal performance was achieved during four cycles. Moreover, according to Fig. 10e, the core is not oxidized because the coating acts as a protector.

3.7. MTT test

The toxicity of $NiFe_2O_4$@Cu(1,2) was examined on MCF7 lung cancer cells. For this purpose, 15×10^3 cells were cultured in each well of a 96-well plate and treated with different concentrations of the compound (1–6 mg/mL). This colorimetric assay was used to determine the cell viability and cytotoxicity within 24 h. Fig. 11 shows the MTT test results of $NiFe_2O_4$@Cu(1) and $NiFe_2O_4$@Cu(2). The cancer cell viability for 1

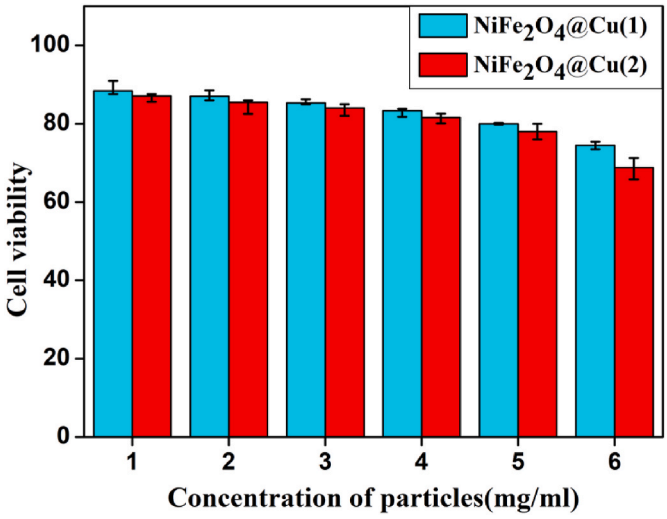

Fig. 11. Cell viability results under different concentrations of NPs over 24 h.

mg/mL concentration of the NiFe2O4@Cu(1) NPs suspension is about 88.6%. It should also be noted that the cancer cell viabilities slowly decrease with increasing concentration of the $NiFe_2O_4$@Cu(1) and

$NiFe_2O_4$@Cu(2) NPs. In other words, even when the concentration of the $NiFe_2O_4$@Cu(1) and $NiFe_2O_4$@Cu(2) NPs is 5 mg/mL, the viabilities of cancer cells are still about 82.8% and 81.4%, respectively. Therefore, the increase in dose and thickness of the copper causes a gradual decrease in cell viability [53]. In general, the low toxicity of these nanoparticles indicates that these nanoparticles can be used in biomedicine [52].

4. Conclusions

In this work, $NiFe_2O_4$ was successfully integrated with copper to prepare core-shell $NiFe_2O_4$@Cu NPs using the co-precipitation method. The obtained XRD patterns confirmed the formation of cubic single-phase NPs with average crystallite sizes in the range of 13.16–15.23 nm based on the Williamson method. Moreover, the TEM and SEM images indicated quasi-spherical crystals in the samples and the formation of core-shell structures. The PL spectrum of the $NiFe_2O_4$@Cu samples exhibited not only less PL intensity but also a shift to higher wavelengths. Since the particle size of the nanomaterials was reduced to less than 25 nm, superparamagnetic properties, low cytotoxicity, and a highly efficient thermal effect were observed. Additionally, these NPs can convert light energy into heat because they show absorption in both the visible and NIR regions. Our results showed that a high concentration of NPs in an aqueous suspension and high-power laser irradiation improve the photothermal effect. Therefore, the photothermal conversion efficiency reached 27.6%. Besides the heating effects, these NPs have more advantages such as low cost and simple synthesis. Consequently, the synthesized $NiFe_2O_4$@Cu NPs are an ideal candidate for use in hyperthermia applications.

Authors' contributions

All authors designed the project; N. Yousefpour Novini, T. Tohidi and K. Jamshidi-Galeh did the experimental design and also carrying out measurements; all authors contributed to the writing of the manuscript.

Ethics approval

This article does not contain any studies with human participants or animals performed by any of the authors.

Funding

This project is supported by Sahand University of Technology with contract number 23681.

Consent to participate

The authors declare the consent to participate.

Consent for publication

The authors declare the consent for publication.

Declaration of competing interest

The authors declare that they have no known competing financial interests or personal relationships that could have appeared to influence the work reported in this paper.

Data availability

Data will be made available on request.

Acknowledgments

Not Applicable.

References

[1] R.-G. Chaudhuri, S. Paria, Core/shell NPs: classes, properties, synthesis mechanisms, characterization, and applications, J Chem Rev 112 (2012) 2373–2433, https://doi.org/10.1021/cr100449n. .
[2] M.-B. Gawande, A. Goswami, T. Asefa, H. Guo, A.-V. Biradar, D.-L. Peng, R. Zboril, R.-S. Varma, Core–shell NPs: synthesis and applications in catalysis and electrocatalysis, J Chem Soci Rev 44 (2015) 7540–7590, https://doi.org/10.1039/C5CS00343A. .
[3] Q. Song, Z.-J. Zhang, Controlled synthesis and magnetic properties of bimagnetic spinel ferrite $CoFe_2O_4$ and $MnFe_2O_4$ nanocrystals with core–shell architecture, J. Chem. Soc. 134 (2012) 10182–10190, https://doi.org/10.1021/ja302856z. .
[4] V. Blanco-Gutiérrez, A. Andrada-Chacón, J. Sánchez-Benítez, E. Urones-Garrote, R. Sáez-Puche, M.-J. Torralvo-Fernández, Superparamagnetic behavior at room temperature through crystal chemistry modification and particle assembly formation: zinc and nickel ferrite systems, J. Phys. Chem. 123 (2019) 16973–16981, https://doi.org/10.1021/jp4052648.
[5] A. Shan, X. Wu, J. Lu, C. Chen, R. Wang, Phase formations and magnetic properties of single crystal nickel ferrite ($NiFe_2O_4$) with different morphologies, CrystEngComm 17 (2015) 1603–1608, https://doi.org/10.1039/c4ce02139h.
[6] P. Mélinon, et al., Engineered inorganic core/shell nanoparticles, Phys. Rep. 543 (2014) 163–197, https://doi.org/10.1016/j.physrep.2014.05.003. .
[7] C.-E. Demirci Donmez, P.-K. Manna, R. Nickel, S. Akturk, J.-V. Lierop, Comparative heating efficiency of cobalt-, manganese-, and nickel-ferrite nanoparticles for a hyperthermia agent in biomedicines, ACS Appl. Mater. Interfaces 11 (2019) 6858–6866, https://doi.org/10.1021/acsami.8b22600.
[8] A.-V. Ambarov, V.-S. Zverev, E.-A. Elfimova, Dynamic response of interacting superparamagnetic particles with aligned easy magnetization axes, J. Magn. Magn Mater. 497 (2020), https://doi.org/10.1016/j.jmmm.2019.166010. .
[9] J. Estelrich, M.-A. Busquets, Iron oxide nanoparticles in photothermal therapy, Molecules 23 (2018) 1567, https://doi.org/10.3390/molecules23071567.
[10] M. Ramazanov, A. Karimova, H. Shirinova, Magnetism for drug delivery, MRI and hyperthermia applications: a review, Biointerface Res Appl Chem 11 (2021) 8654–8668, https://doi.org/10.33263/BRIAC112.86548668.
[11] S.-W. Lee, S. Bae, Y. Takemura, E. Yamashita, J. Kunisaki, S. Zurn, C.-S. Kim, Magnetic properties, self-temperature rising characteristics, and biocompatibility of $NiFe_2O_4$ nanoparticles for hyperthermia applications, IEEE Trans. Magn. 42 (2006) 2833–2835, https://doi.org/10.1109/TMAG.2006.879142. .
[12] C.-E. Demirci Donmez, P.-K. Manna, R. Nickel, S. Akturk, J. van Lierop, Comparative heating efficiency of cobalt-, manganese-, and nickel-ferrite nanoparticles for a hyperthermia agent in biomedicines, ACS Appl. Mater. Interfaces 11 (6858 6866) (2019), https://doi.org/10.1021/acsami.8b22600.
[13] S. Fu, Y. Man, F. Jia, Photothermal effect of superparamagnetic Fe_3O_4 nanoparticles irradiated by near-infrared laser, J Nano 34 (2020) 4078–4088, https://doi.org/10.1155/2020/2832347. .
[14] F. Ghorbani, A. Imanparast, F. Hataminia, A. Sazgarnia, A novel nano-superparamagnetic agent for photodynamic and photothermal therapies: an in-vitro study, Photodiagnosis Photodyn. Ther. 23 (2018) 314–324, https://doi.org/10.1016/j.pdpdt.2018.07.008. .
[15] P. Prakash, G. Srimathveeravalli, Principles and Technologies for Electromagnetic Energy Based Therapies, Academic Press, 2021.
[16] Y. Yagawa, K. Tanigawa, Y. Kobayashi, M. Yamamoto, Cancer immunity and therapy using hyperthermia with immunotherapy, radiotherapy, chemotherapy, and surgery, J Cancer Metastasis and Treatment 3 (2017) 218–230, https://doi.org/10.20517/2394-4722.2017.35. .
[17] M.-A. Busquets, J.-M. Fernández-Pradas, P. Serra, J. Estelrich, Superparamagnetic nanoparticles with efficient near-infrared photothermal effect at the second biological window, Molecules 25 (2020) 5315, https://doi.org/10.3390/molecules25225315.
[18] J.-L. Roti, Cellular responses to hyperthermia (40–46 C): cell killing and molecular events, Int J hyperthermia 24 (2008) 3–15, https://doi.org/10.1080/02656730701769841. .
[19] A. Asrar, Z. Sobhani, M.-A. Behnam, Melanoma cancer therapy using PEGylated nanoparticles and semiconductor laser, Adv. Pharmaceut. Bull. 12 (2022) 524–530, https://doi.org/10.34172/apb.2022.055. doi.
[20] W. Li, H. Qi, F. Guo, X. Niu, Y. Du, Y. Chen, $NiFe_2O_4$ nanoparticles supported on cotton-based carbon fibers and their application as a novel broadband microwave absorbent, RSC Adv. 9 (2019) 29959–29966, https://doi.org/10.1039/C9RA05844C. .
[21] V. Blanco-Gutiérrez, A. Andrada-Chacón, J. Sánchez-Benítez, E. Urones-Garrote, R. Sáez-Puche, M.-J. Torralvo-Fernández, Superparamagnetic behavior at room temperature through crystal chemistry modification and particle assembly formation: zinc and nickel ferrite systems, J. Phys. Chem. C 123 (2019) 16973–16981, https://doi.org/10.1021/acs.jpcc.9b01898. .
[22] G. Rana, P. Dhiman, A. Kumar, D.-V.-N. Vo, G. Sharma, S. Sharma, M. Naushad, Recent advances on nickel nano-ferrite: a review on processing techniques, properties and diverse applications, Chem. Eng. Res. Des. 175 (2021) 182–208, https://doi.org/10.1016/j.cherd.2021.08.040.

[23] V.-V. Mody, A. Singh, B. Wesley, Basics of magnetic nanoparticles for their application in the field of magnetic fluid hyperthermia, Eur. J. Nanomed. 5 (2013) 11–21, https://doi.org/10.1515/ejnm-2012-0008. .
[24] M. Hjiri, N.-H. Alonizan, M.-M. Althubayti, S. Alshammari, H. Besbes, M.-S. Aida, Preparation and photoluminescence of $NiFe_2O_4$ nanoparticles, J Sci Mater 30 (2019) 15379–15387, https://doi.org/10.1007/s10854-019-01914-9.
[25] N. Zhang, Y. Gao, H. Zhang, X. Feng, H. Cai, Y. Liu, Preparation and characterization of core–shell structure of SiO_2@Cu antibacterial agent, Colloids Surf., B 81 (2010) 537–543, https://doi.org/10.1016/j.colsurfb.2010.07.054. .
[26] Q. Tian, et al., Sub-10 nm Fe_3O_4@ $Cu_{2-x}S$ core–shell nanoparticles for dual-modal imaging and photothermal therapy, J. Am. Chem. Soc. 135 (2013) 8571–8577, https://doi.org/10.1021/ja4013497. .
[27] X. Gao, P. Zhang, K. Du, M. Zhang, D. Wen, Y. Lu, J. Feng, H. Zhang, Near-infrared-light-responsive copper oxide nanoparticles as efficient theranostic nanoagents for photothermal tumor ablation, ACS Appl. Bio Mater. 4 (2021) 5266–5275, https://doi.org/10.1021/acsabm.1c00410. .
[28] D. Saykova, S. Saikova, Y. Mikhlin, M. Panteleeva, R. Ivantsov, E. Belova, Synthesis and characterization of core–shell magnetic nanoparticles $NiFe_2O_4$@Au, Metals 10 (2020) 1075, https://doi.org/10.3390/met10081075.
[29] C. Koo, et al., Magnetic and near-infrared derived heating characteristics of dimercaptosuccinic acid coated uniform Fe@Fe_3O_4 core–shell nanoparticles, Nano Converg 7 (2020) 1–9, https://doi.org/10.1186/s40580-020-00229-4.
[30] R. Betancourt-Galindo, P.-Y. Reyes-Rodriguez, B.-A. Puente-Urbina, C.-A. Avila-Orta, O.-S. Rodríguez-Fernández, G. Cadenas-Pliego, L.-A. García-Cerda, Synthesis of copper nanoparticles by thermal decomposition and their antimicrobial properties, J. Nanomater. 2014 (10) (2014), https://doi.org/10.1155/2013/980545.
[31] V.-S. Vinila, X-ray diffraction analysis of nano crystalline ceramic PbBaTiO3, Cryst. Struct. Theor. Appl. 3 (2014) 57–65, https://doi.org/10.4236/csta.2014.33007.
[32] H.-S. Aziz, R.-A. Khan, F. Shah, B. Ismail, J. Nisar, S.-M. Shah, A. Rahim, A.-R. Khan, Improved electrical, dielectric and magnetic properties of Al-Sm co-doped NiFe2O4 spinel ferrites nanoparticles, Mater. Sci. Eng. B 243 (2019) 47–53, https://doi.org/10.1016/j.mseb.2019.03.021. .
[33] B. Zeynizadeh, I. Mohammadzadeh, Z. Shokri, S.-A. Hosseini, Synthesis and characterization of $NiFe_2O_4$@Cu nanoparticles as a magnetically recoverable catalyst for reduction of nitroarenes to arylamines with NaBH4, J. Colloid Interface Sci. 500 (2017) 285–293, https://doi.org/10.1016/j.jcis.2017.03.030. .
[34] R. E-Nimshi, J. J-Vijaya, B. Al-Najar, L. Hazeem, M. Bououdina, L. J-Kennedy, K. Kombaiah, S. Bellucci, Multifunctional core-shell $NiFe_2O_4$ shield with TiO_2/rGO nanostructures for biomedical and environmental applications, Bioinorg. Chem. 1 (2022), https://doi.org/10.1155/2022/4805490, 21.
[35] F. Ke, L.-G. Qiu, Y.-P. Yuan, X. Jiang, J.-F. Zhu, Fe_3O_4@MOF core–shell magnetic microspheres with a designable metal–organic framework shell, J. Mater. Chem. 22 (2012) 9497–9500, https://doi.org/10.1039/C2JM31167D. .
[36] I.-M. Obaidat, C. Nayek, K. Manna, Investigating the role of shell thickness and field cooling on saturation magnetization and its temperature dependence in Fe_3O_4/γ-Fe_2O_3 Core/Shell nanoparticles, Appl. Sci. 7 (2017) 1269, https://doi.org/10.3390/app7121269.
[37] W.-E. Pottker, et al., Influence of order-disorder effects on the magnetic and optical properties of $NiFe_2O_4$ nanoparticles, Ceram. Int. 44 (2018) 17290–17297, https://doi.org/10.1016/j.ceramint.2018.06.190. .
[38] X. Zhao, Y.-L. Zhang, X.-X. Wang, H.-L. Shi, W.-Z. Wang, M.-S. Cao, Enhanced microwave absorption properties of $NiFe_2O_4$ nanocrystal deposited reduced graphene oxides, J. Mater. Sci. Mater. Electron. 27 (2016) 11518–11523, https://doi.org/10.1007/s10854-016-5280-0.
[39] G. Cheng, A.-R. Hight Walker, Transmission electron microscopy characterization of colloidal copper nanoparticles and their chemical reactivity, Anal. Bioanal. Chem. 396 (2010) 1057–1069, https://doi.org/10.1007/s00216-009-3203-0.
[40] A. Azab, S. Albaaj, Effect of grinding time on the structural and magnetic properties of ultrafine $Ni_{0.7}Zn_{0.3}Fe_2O_4$, J Ovonic Res 11 (2015) 195–201.
[41] K. Vepulanont, et al., Nickel ferrite ceramics: combustion synthesis, sintering, characterization, and magnetic and electrical properties, J Asian Ceram Soc 9 (2021) 639–651, https://doi.org/10.1080/21870764.2021.1907031. .
[42] Budhiraja N. Sapna, V. Kumar, S.-K. Singh, Tailoring the structural, optical and magnetic properties of $NiFe_2O_4$ by varying annealing temperature, J. Supercond. Nov. Magnetism 31 (2018) 2647–2654, https://doi.org/10.1007/s10948-017-4529-z. .
[43] S. Zhang, J. Ye, Z. Liu, H. Lu, S. Shi, Y. Qi, G. Ning, Superior antibacterial activity of Fe_3O_4@copper(ii) metal–organic framework core–shell magnetic microspheres, Dalton Trans. 49 (2020) 13044–13051, https://doi.org/10.1039/D0DT02417A.
[44] H. Guan, J. Wang, S. Tan, Q. Han, Q. Liang, M. Ding, A facile method to synthesize magnetic nanoparticles chelated with copper (II) for selective adsorption of bovine hemoglobin, Kor. J. Chem. Eng. 37 (2020) 1097–1106, https://doi.org/10.1007/s11814-020-0532-3. .
[45] T.-A. Taha, A.-A. Azab, M.-A. Sebak, Glycerol-assisted sol-gel synthesis, optical, and magnetic properties of $NiFe_2O_4$ nanoparticles, J. Mol. Struct. 1181 (2019) 14–18, https://doi.org/10.1016/j.molstruc.2018.12.075.
[46] I.-L. Soroka, A. Shchukarev, M. Jonsson, N.-V. Tarakina, P.-A. Korzhavyi, Cuprous hydroxide in a solid form: does it exist? Dalton Trans. 42 (2013) 9585–9594, https://doi.org/10.1039/C3DT50351H.
[47] M.I.S.M.H. Tan, A.F. Omar, M. Rashid, U. Hashim, VIS-NIR spectral and particles distribution of Au, Ag, Cu, Al and Ni nanoparticles synthesized in distilled water using laser ablation, Results Phys. 14 (2019), 102497, https://doi.org/10.1016/j.rinp.2019.102497. .
[48] D. Zhang, X. Pu, K. Du, Y.-M. Yu, J.-J. Shim, P. Cai, S. Kim, H.-J. Seo, Combustion synthesis of magnetic Ag/NiFe2O4 composites with enhanced visible-light photocatalytic properties, Sep. Purif. Technol. 137 (2014) 82–85, https://doi.org/10.1016/j.seppur.2014.09.025.
[49] P.-A. Udhaya, M. Meena, Albumen assisted green synthesis of $NiFe_2O_4$ nanoparticles and their physico-chemical properties, Mater. Today Proc. 9 (2019) 528–534, https://doi.org/10.1016/j.matpr.2018.10.372.
[50] B.-C. Reddy, et al., Synthesis and characterization of multi-functional nickel ferrite nano-particles for X-ray/gamma radiation shielding, display and antimicrobial applications, J. Phys. Chem. Solid. 159 (2021), 110260, https://doi.org/10.1016/j.jpcs.2021.110260.
[51] A. Espinosa, J. Kolosnjaj-Tabi, A. Abou-Hassan, A. Plan Sangnier, A. Curcio, A. K. Silva, C. Wilhelm, Magnetic (hyper) thermia or photothermia? Progressive comparison of iron oxide and gold nanoparticles heating in water, in cells, and in vivo, Adv. Funct. Mater. 28 (37) (2018), 1803660, https://doi.org/10.1002/adfm.201803660.
[52] S. He, et al., Maximizing specific loss power for magnetic hyperthermia by hard–soft mixed ferrites, Small 14 (2018), 1800135, https://doi.org/10.1002/smll.201800135.
[53] P.-B. Tchounwou, C. Newsome, J. Williams, K. Glass, Copper-induced cytotoxicity and transcriptional activation of stress genes in human liver carcinoma (HepG2) cells, Metal Ions Biol. Med. 10 (2008) 285–290.